Anisotropy of the electron component in a cylindrical magnetron discharge. II. Application to real magnetron discharge

I. A. Porokhova,[1,2] Yu. B. Golubovskii,[1] and J. F. Behnke[2]

[1]*Saint-Petersburg State University, Ulianovskaia, 1, 198504, St. Petersburg, Russia*
[2]*EMA-University, Greifswald, Domstrasse 10a, 17487 Greifswald, Germany*

The physical processes occurring in electrode regions and the positive column of a cylindrical magnetron discharge in crossed electric and magnetic fields are investigated based on the solution of the Boltzmann kinetic equation by a multiterm decomposition of the electron phase space distribution function in terms of spherical tensors. The influence of the distribution function anisotropy on the absolute values and radial profiles of the electron density and rates of various transport and collision processes is analyzed. The spiral lines for the directed particle and energy transport are obtained to illustrate the anisotropy effects in dependence on the magnetic field. The electron equipressure surfaces are constructed in the form of ellipsoids of pressure and their transformation in the cathode and anode regions is studied. A strong anisotropy of the energy flux tensor in contrast to a weak anisotropy of the momentum flux density tensor is found. Particular results are obtained for the cylindrical magnetron discharge in argon at pressure 3 Pa, current 200 mA, and magnetic fields ranging within 100 and 400 G.

PACS number(s): 52.25.Dg, 52.25.Fi, 52.25.Xz

I. INTRODUCTION

Magnetron discharge in the form of a coaxial cylindrical inner cathode and outer anode with radial electric and axial magnetic fields was studied experimentally and theoretically [1–5]. Electron distribution measurements were performed in dependence on the radial position and magnetic field strengths, as well as measurements of the electron density and mean energy, potential profiles, and radial distribution of metastable, resonance, and radiating atoms. On the other hand, the processes occurring in a cylindrical magnetron discharge were simulated by various methods including particle-in-cell Monte-Carlo collisions (MCC) [4] and kinetic self-consistent modeling [5].

In our previous paper [5] a self-consistent model of a magnetron discharge was developed based on the Boltzmann kinetic equation solution in the two-term approximation with account of the effects of electric and magnetic fields, spatial gradients, and important collision processes. A specific deformation of the distribution function from cathode to anode was demonstrated, and macroscopic quantities, such as electron density and mean energy, electron and ion radial current densities were obtained. Description of the electron component was supplemented by equations for the ions and field. Subsequently, the edge effects connected with the finite length of magnetron and the presence of the axial electric field and plasma axial inhomogeneities were taken into account [6]. Additionally, the metastable and resonance atom formation processes in similar discharges were discussed [7]. Results were compared with experiments.

The present paper reports on investigations of the electron plasma component in a cylindrical magnetron discharge, obtained from the solution of the Boltzmann kinetic equation using the multiterm expansion discussed in the preceding paper [8]. The multiterm approach permits us to consider various phenomena connected with the distribution function

anisotropy which is caused by strong electric fields in the cathode region, and by absorption of electrons on the anode in the anode region. A uniform description of the positive column and electrode region, as well as the possibility to obtain detailed information about the distribution function and macroscopic quantities, can be attributed to advantages of the method. The general equations formulated in the previous paper [8] were applied to real operating conditions of an argon cylindrical magnetron discharge, and particular results for the terms of the electron distribution function and macroscopic quantities responsible for transport of particles, momentum, and energy obtained. The radial evolution of these quantities is considered in dependence on magnetic field strength.

II. RADIAL POTENTIAL PROFILES AND DISTRIBUTION FUNCTIONS

The theory of the multiterm representation of the Boltzmann kinetic equation in terms of spherical tensors [8,9] is applied to study the magnetron discharge between two cylindrical coaxial electrodes of length $L = 30$ cm with the radii of the inner cathode $R_C = 0.9$ cm and the outer anode $R_A = 3$ cm in argon at neutral gas pressure 3 Pa, current $i = 200$ mA, and magnetic fields $B = 100$, 150, 200, and 400 G. This corresponds to the range of reduced magnetic fields from $B/N = 12\,500$ to 50 000 Hx. The magnetic field is created by coils with current; it is uniform along the axis of the cylinder in contrast to planar configurations, where the magnetic field is strongly inhomogeneous.

This type of discharge has been studied experimentally in a series of papers [1–3]. The radial distribution of the electron density as well as the difference of the potentials between the cathode and anode, V_{AC}, are the quantities measured accurately. To calculate the electron distribution function data on the radial profiles of the potential are
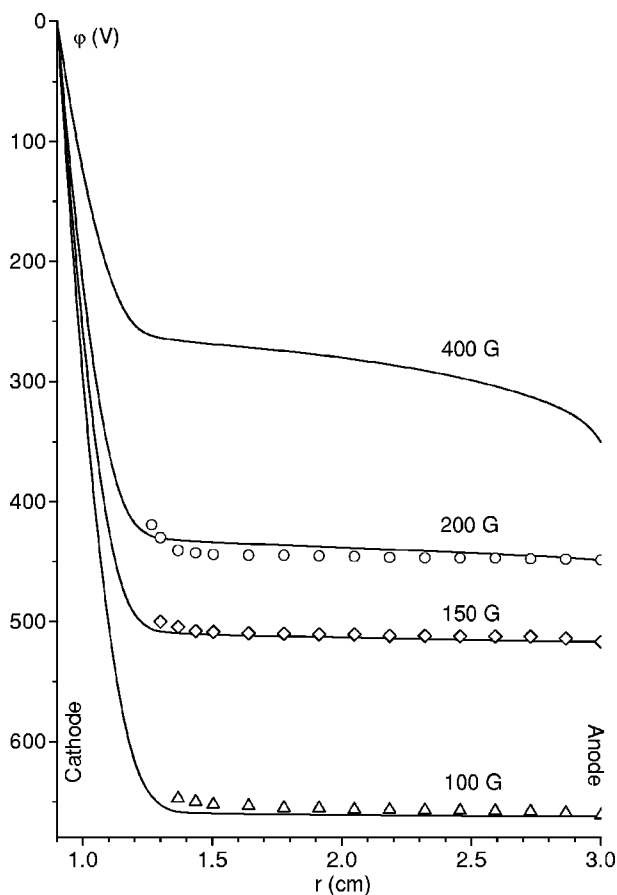
FIG. 1. Radial distributions of the potential in dependence on magnetic field strength. Symbols are the experimentally measured floating potentials. The potential differences between cathode and anode correspond to experimentally measured values.
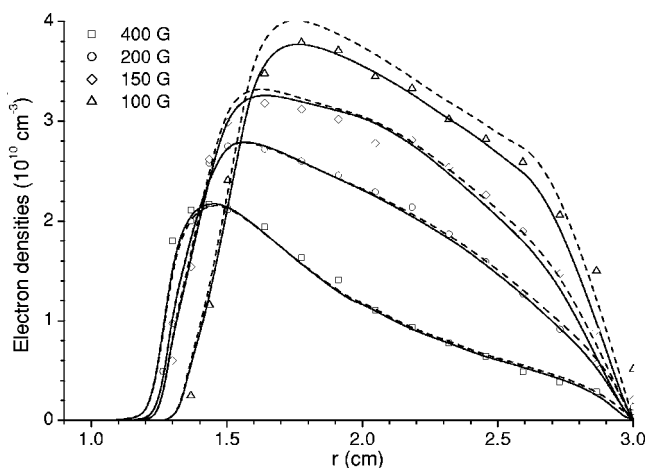

FIG. 2. Radial profiles of the electron density. Full and broken lines show the multiterm and two-term approximation results, respectively. Symbols are the data from experiments.

needed. These cannot be obtained with the required accuracy from direct probe measurements due to the large field gradient in the electrode region and positive column, and errors in determination of the plasma potential from the second derivative of the probe current. In further calculations the radial profile of the electric field strength was chosen in such a way that the voltage on the discharge gap V_{AC} corresponds to the experimentally measured value, and the electron distribution function calculated in this field gives the absolute values and radial profile of the electron density equal to the experimentally measured density of electrons.

The radial profiles of the potentials are shown in Fig. 1, and the radial distributions of the electron densities formed in these potential fields are presented in Fig. 2. The good agreement between the measured [3] and calculated values of the absolute electron density indicates that the chosen potential profiles correspond to the real ones. There is also agreement between the chosen radial distribution of the potential and the measured floating potentials (symbols in Fig. 1). The plasma potential has also been measured in the experiments but with less accuracy. The specific structure of the potential distributions is connected with the presence of strong electric fields in the cathode region and weak fields in the positive column. An increase in the electric field strength in the positive column and anode region is observed with increasing

magnetic field. The fall of the potential between cathode and anode decreases noticeably from 660 V at $B=100$ G to 350 V at $B=400$ G.

The distribution functions formed in these potentials were obtained by using the spherical tensor multiterm representation described in the preceding paper [8]. The system of ordinary differential equations (25)–(34) [8] was written in finite differences on a grid nonequidistant in both total energy and radius coordinates. A numerical method for split boundary value problems [10] was used, in which the indices of the required functions are shifted in dependence on the boundary conditions set on the right or left boundaries. This method provided stability of the numerical scheme with the boundary conditions being appropriately set for expansion coefficients with even and odd l indexes. The obtained system of linear equations for ten components of the distribution function was solved at constant total energy for each energy grid point. The solution region of the system and boundary conditions were discussed in the preceding paper. The resultant distribution functions were normalized by the value of electron current density at the anode ej_e. At the anode the electron current density equals the total current density ej_0 related to the discharge current i according to

$$i = 2\pi r e j_0(r) L.$$

The isotropic part of the distribution function $f_0(U,r)$ is shown in Fig. 3 in dependence on the kinetic energy U and radial coordinate r for $B=100$ and 400 G. The electron densities calculated using the isotropic distributions $f_0(U,r)$ are represented in Fig. 2. The relative error $\delta_n = |n^{(4)}(r) - n^{(2)}(r)|/n^{(4)}(r)$, estimated according to the accuracy criterion [11] for electron densities calculated in the two-term $[n^{(2)}(r)]$ and four-term $[n^{(4)}(r)]$ approximations, equals 0.05 in the positive column and increases up to the magnitude 0.5 near both electrodes at the lowest magnetic field. This error, as expected, decreases with increasing magnetic field strength.

In calculating the distribution function an initial Gaussian-like beam of high-energy electrons was assumed to
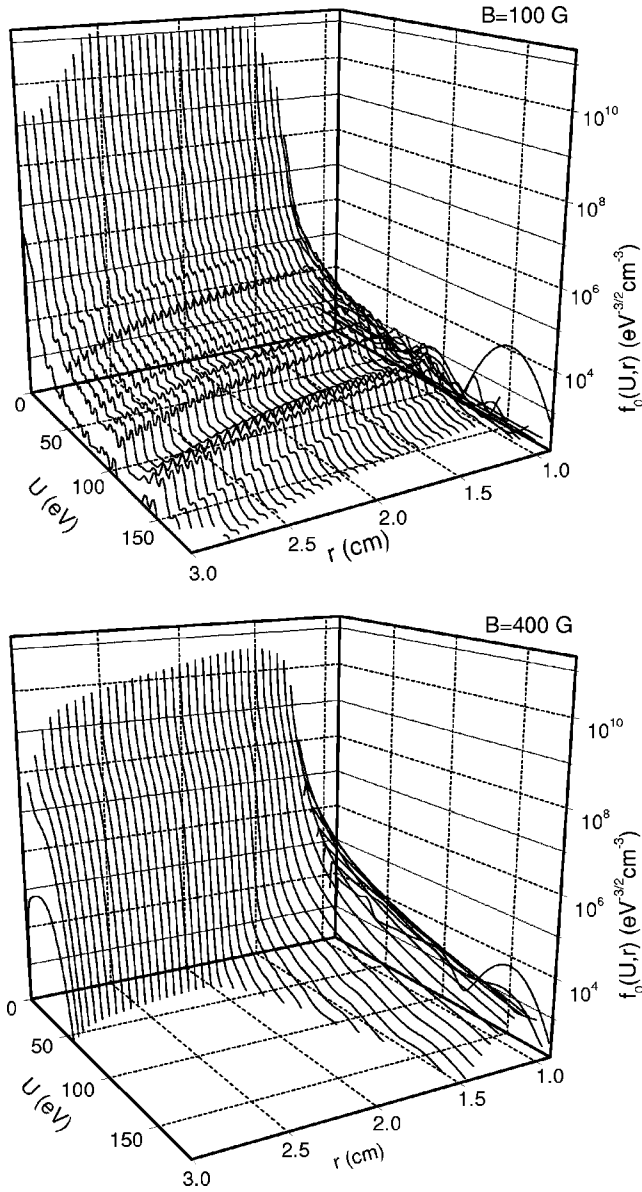
FIG. 3. Isotropic part of the electron distribution function $f_0(U,r)$ at magnetic field strengths $B=100$ and 400 G. $R_C=0.9$ cm, $R_A=3$ cm.

be ejected from cathode into the plasma. Specific deformations of the distribution function with increasing magnetic field can be seen in Fig. 3. At weak magnetic fields (100 G) a pronounced undulating structure is formed, that moves in an ordered way along the radius and energy and reaches the anode. This structure is connected with a relaxation of the initial beam of electrons in inelastic and ionizing collisions. The distribution function tail is extended to very high kinetic energies, so that the electron mean energy reaches 280 eV in the cathode region and then decreases to 1.5 eV in the positive column. At large magnetic field (400 G) this undulating structure vanishes. The distribution function on approaching the anode decreases rapidly, and the mean electron energy varies from 100 eV near the cathode to 4 eV in the quasineutral plasma. The difference in the electron mean energies under two magnetic field conditions is stipulated by changes

in the potential profiles (Fig. 1) in dependence on magnetic field. The electric field strength in the cathode region at weak magnetic fields is remarkably larger than that at the strong fields, but in the positive column the situation is opposite.

The undulating structure formation in the cathode region has been discussed in detail in [5]. At weak magnetic fields the structure with peaks in the distribution function is transported through the positive column to the anode. At strong magnetic fields (e.g., $B=400$ G, Fig. 3) the structure is smoothed. This effect can be explained by the decrease in the energy relaxation length with increasing magnetic field. The electron distribution function relaxation occurs on the length shortest of $\lambda_{inel} \approx U_{ex}/(eE)$ and $\lambda_\varepsilon \approx (M/m_e)^{1/2} r_L$ [6], where r_L is the radius of electron cyclotron motion, U_{ex} is the excitation threshold, and m_e and M are the electron and atom masses. At weak magnetic fields these lengths are comparable to or even exceed the magnetron dimensions; therefore the peaks in the electron distribution persist in the whole gap. With increasing magnetic field, both relaxation lengths shorten due to the increase of both the electric and magnetic fields, thus resulting in the distribution localization and flattening.

Similar dependencies are observed in the behaviour of the higher-order terms of the distribution function, for example on the function $f_1 = \mathrm{Re}(F_{1,1})$ (Fig. 4). The terms with higher-l indices oscillate rapidly especially at weak magnetic fields, so that their visual three-dimensional presentation is difficult. The influence of the higher-order terms will be illustrated on macroscopic quantities.

III. BALANCE EQUATIONS

The balance equations identically follow from the Boltzmann kinetic equation and must hold for any method of distribution function decomposition. In what follows, we use the same designations as in the previous paper [8].

With respect to the cylindrical magnetron discharge configuration the balance equations for the electrons with charge $-e$ have the following forms:
the particle balance equation

$$\frac{1}{r}\frac{\partial}{\partial r} r j_r = I_d ; \tag{1}$$

the energy balance equation

$$\frac{1}{r}\frac{\partial}{\partial r} r j_{ur} + eE j_r = -(H_{el} + H_{ex} + H_{io}); \tag{2}$$

the radial momentum balance equation

$$\frac{\partial}{\partial r} p + neE + ne[\mathbf{v} \times \mathbf{B}]_r + \frac{1}{r^2}\frac{\partial}{\partial r} r^2 \Pi_{rr} + \frac{\Pi_{zz}}{r} = -R_r^{(c)}; \tag{3}$$

and the azimuth momentum balance equation

$$ne[\mathbf{v} \times \mathbf{B}]_\varphi + \frac{1}{r^2}\frac{\partial}{\partial r} r^2 \Pi_{r\varphi} = -R_\varphi^{(c)}. \tag{4}$$

The particle balance equation (1), or equation of continuity, reads that the gain of particles by ionizing collisions
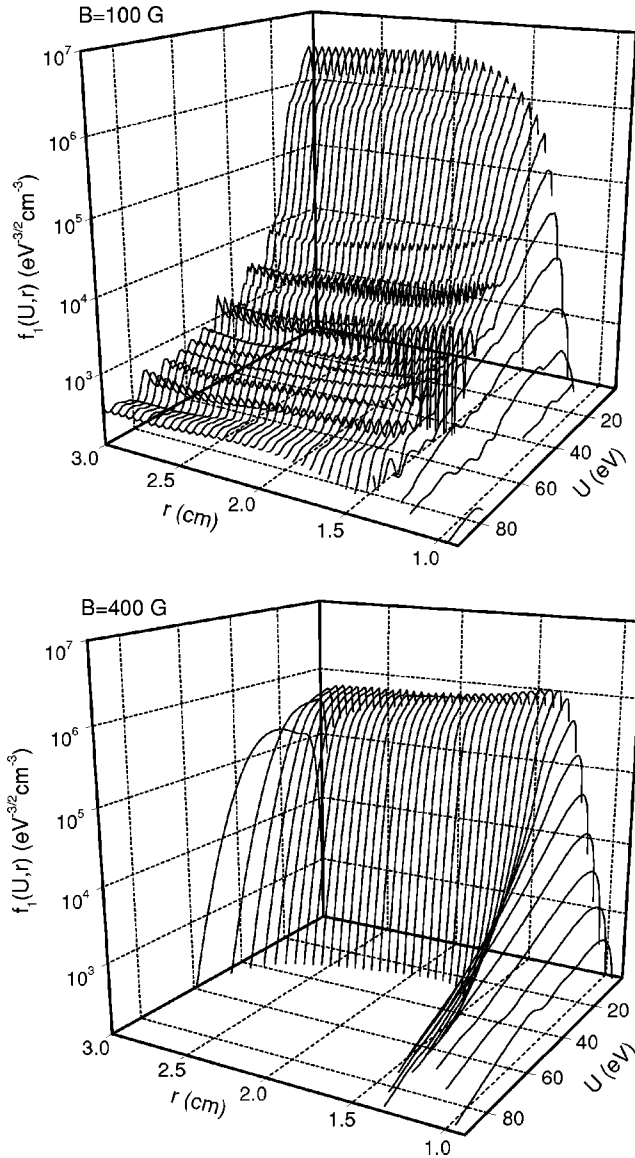
FIG. 4. Anisotropic part of the electron distribution function $f_1(U, r)$ at magnetic field strengths $B = 100$ and 400 G.

$$I_d(r) = \sqrt{\frac{2}{m_e}} \int_{U_{di}}^{\infty} UNQ^{di} f_0(U, r) dU \qquad (5)$$

causes equal divergence of the particle flux (j_r) in the radial direction,

$$j_r(r) = \frac{1}{3} \sqrt{\frac{2}{m_e}} \int_0^{\infty} \mathrm{Re}(F_{1,1}) U \, dU. \qquad (6)$$

Here, I_d is the direct ionization rate, N is the atom density, Q^{di} is the ionization cross section, and U_{di} is the ionization potential. $F_{l,m}$ are the coefficients for the distribution function decomposition, where $l = 0, 1, 2, 3$ and $m = -l, \dots, l$. The component $F_{0,0}$ corresponds to the isotropic distribution; $\mathrm{Re}(F_{1,1})$ and $\mathrm{Im}(F_{1,1})$ are the analogs for radial and azimuth anisotropic distribution in the two-term approximation.

According to the energy balance equation (2) the difference between the power gain (eEj_r) and power losses in elastic (H_{el}), inelastic (H_{ex}), and ionizing (H_{io}) collisions

$$H_{el} = 2 \frac{m_e}{M} \sqrt{\frac{2}{m_e}} \int_0^{\infty} U^2 NQ^d f_0(U, r) dU,$$

$$H_{ex} = U_{ex} \sqrt{\frac{2}{m_e}} \int_{U_{ex}}^{\infty} UNQ^{ex} f_0(U, r) dU,$$

$$H_{io} = U_{di} I_d$$

is compensated for by the divergence of the radial energy flux

$$j_{ur} = \frac{1}{3} \sqrt{\frac{2}{m_e}} \int_0^{\infty} \mathrm{Re}(F_{1,1}) U^2 dU.$$

Here, Q^d and Q^{ex} are the momentum transfer and total inelastic cross sections, and U_{ex} is the excitation threshold.

The main contributions to the radial momentum balance equation (3) are connected with the particle acceleration due to the electric field (eEn), the gradient of pressure

$$p = (2/3)nU_e, \qquad (7)$$

where n is the electron density and U_e is the mean energy,

$$n = \int_0^{\infty} f_0 U^{1/2} dU, \quad nU_e = \int_0^{\infty} f_0 U^{3/2} dU,$$

and radial motion due to the action of the Lorentzian force

$$ne[\mathbf{v} \times \mathbf{B}]_r = m_e \Omega j_{\varphi},$$

where the azimuth particle flux is

$$j_{\varphi} = -\frac{1}{3} \sqrt{\frac{2}{m_e}} \int_0^{\infty} \mathrm{Im}(F_{1,1}) U \, dU \qquad (8)$$

and $\Omega = eB/m_e$ is the frequency of electron cyclotron motion.

The rate of momentum loss due to collisions

$$R_r^{(c)} = \frac{2}{3} \int_0^{\infty} U^{3/2} NQ_\Sigma \, \mathrm{Re}(F_{1,1}) dU$$

and the terms containing the second rank tensor components

$$\Pi_{rr} = \frac{2}{5} \int_0^{\infty} U^{3/2} [\mathrm{Re}(F_{2,2}) - F_{2,0}/3] dU, \qquad (9)$$

$$\Pi_{zz} = \frac{4}{15} \int_0^{\infty} U^{3/2} F_{2,0} dU \qquad (10)$$

contribute a little Here, $Q_\Sigma = Q^d + Q^{ex} + Q^{di}$.

The balance equation for the momentum transport in the azimuth direction (4) suggests an equality of the Lorentzian force

$$ne[\mathbf{v} \times \mathbf{B}]_{\varphi} = m_e \Omega j_r$$

to the sum of the azimuth friction force

$$R_\varphi^{(c)} = \frac{2}{3} \int_0^\infty U^{3/2} N Q_\Sigma \, \mathrm{Im}(F_{1,1}) dU$$

and the gradient of the corresponding component of the anisotropic pressure tensor

$$\Pi_{r\varphi} = -\frac{2}{5} \int_0^\infty U^{3/2} \, \mathrm{Im}(F_{2,2}) dU. \qquad (11)$$

As it is seen from the balance equations for the scalar quantities (1) and (2) the gains of the particles and energy in the elementary volume are compensated for by the fluxes going in the radial direction only. The vector components of the momentum transport (3) and (4) and the tensor components of the energy flux transport are balanced in both the radial and azimuth directions.

IV. EFFECT OF MAGNETIC FIELD ON THE TRANSPORT QUANTITIES

The physical pattern of the processes occurring in the cylindrical magnetron discharge in dependence on magnetic field strength can be illustrated on macroscopic quantities calculated using the corresponding expansion coefficients of the obtained distribution functions.

A. Transport of particles

The radial dependencies of the ionization rate (5) and radial (6) and azimuth (8) components of the electron flux density are shown in Fig. 5. Broken lines illustrate the results obtained in the two-term approximation.

The ionization rate strongly increases from the cathode through the cathode fall and reaches its maximum in the region of transition from strong electric fields in the cathode region to weak fields in the positive column; then it decreases smoothly toward the anode. A noticeable increase of the ionization rate in the anode region at $B=400$ G is caused by the presence of an explicit anode fall formed at large magnetic field strengths (Fig. 1). To avoid encumbering figures, the two-term approximations results are given for weak (100 G) and strong (400 G) magnetic fields only. The higher-order terms do not have a strong influence on the values of ionization rate. The relative error δ_I, estimated for ionization rates in the two- and four-term approximations by analogy to δ_n discussed above, amounts to 0.15 at $B=100$ G and $r<1.5$ cm and decreases toward the anode rapidly. At $B=400$ G this error does not exceed the value $\delta_I=0.06$.

According to Fig. 5, the azimuth electron flux considerably exceeds the radial one. Similar proportion of the radial and azimuth components of the particle flux vector results in directed motion of the electrons along spiral trajectories in transverse sections of cylindrical magnetron. These trajectories can be easily computed from the equations of directed motion written in the form

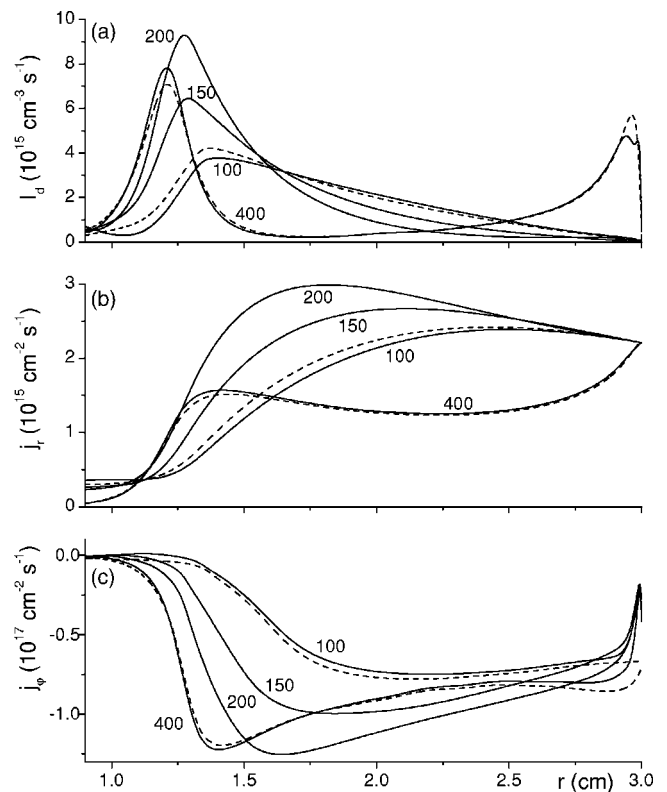$$\frac{dr}{dt} = u_r(r), \qquad r|_{t=0} = R_C,$$

FIG. 5. Radial profiles of the direct ionization rate I_d (a), radial electron flux j_r (b), and azimuth electron flux j_φ (c). Full and broken lines show the multiterm and two-term approximation results, respectively. Numbers are the magnetic field strengths in gauss.

$$\frac{d\varphi}{dt} = \frac{u_\varphi(r)}{r}, \qquad \varphi|_{t=0} = \varphi_0,$$

where $u_r(r)=j_r(r)/n(r)$ and $u_\varphi(r)=j_\varphi(r)/n(r)$ are the radial and azimuth components of the electron directed velocity and φ_0 is the initial phase.

Trajectories of the electron directed motion from cathode to anode are shown in Fig. 6 under various magnetic field conditions. These trajectories coincide with the lines of current, a tangent to the curves at each point gives the direction of the electron flux vector **j**, with modulus $j=(j_r^2+j_\varphi^2)^{1/2}$. The discharge current i is transported by the radial component j_r only. The figure shows that the number of rotations in the plane (r,φ) increases with the increase of magnetic field. The time required for an electron to travel the distance from cathode to anode amounts to $\sim 10-20 \ \mu$s depending on magnetic field.

An effect of strong anisotropy on the lines of current should be noted for the cathode region at $B=100$ G. There is a short range of radial positions in this region, where j_φ becomes positive (Fig. 5), which results in distortions of the electron trajectories. A more comprehensive discussion of this phenomenon requires taking account of higher-order expansion coefficients for the distribution function.

Under the present conditions the magnetic field has negligible effect on the ion motion, thus the azimuth component of the directed velocity is much smaller than the radial one.
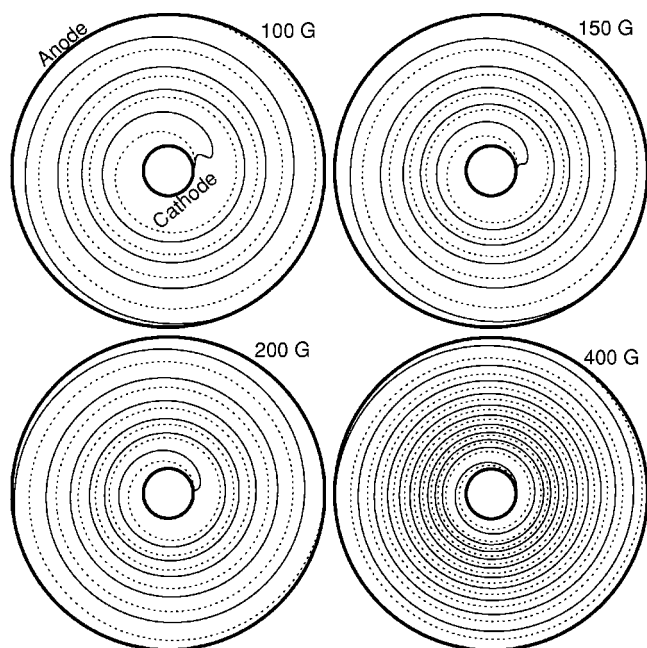
FIG. 6. Lines of electron current in the plane z=const of the cylindrical magnetron discharge. Multiterm approximation (full lines) is compared with the two-term approximation (broken lines).

The above considered directed motion of the charged particles is a consequence of collisions in the plasma. In the hypothetical case of a collisionless motion, both electrons and ions will travel along circles due to the electric drift in the crossed fields; the radial component of their directed velocities will equal zero.

B. Transport of momentum

In both the two-term and multiterm approximations, the forces $en(E+[\mathbf{v}\times\mathbf{B}]_r)$ acting on electrons in an elementary volume and appearing in the radial momentum balance equation (3) are compensated for mainly by the gradient of isotropic pressure of the electrons p, Eq. (7). These quantities are represented in Fig. 7. Other terms in Eq. (3) are two or three orders of magnitude smaller with the exception of their values in the electrode regions. A formation of a pronounced maximum in the force term neE in the transition range between the cathode region and positive column is stipulated by a decrease of the electric field strength and increase of electron density. At magnetic field strengths of the order of 100–150 G this maximum is equalized by the isotropic pressure gradient; at higher values of the magnetic field the contribution of the Lorentzian force increases. The peaks of ionization rates clearly seen in Fig. 5(a) are also connected with this maximum. It should be noted that the nonlocal character of the distribution function formation leads to significant broadening of ionization rate profiles.

According to calculation results of the azimuth momentum balance equation terms, the Lorentzian force in the azimuth direction $ne[\mathbf{v}\times\mathbf{B}]_\varphi=m\Omega j_r$ is compensated for by the force of friction $R_\varphi^{(c)}$ at all radial positions except for the anode region where the electron pressure anisotropy [second
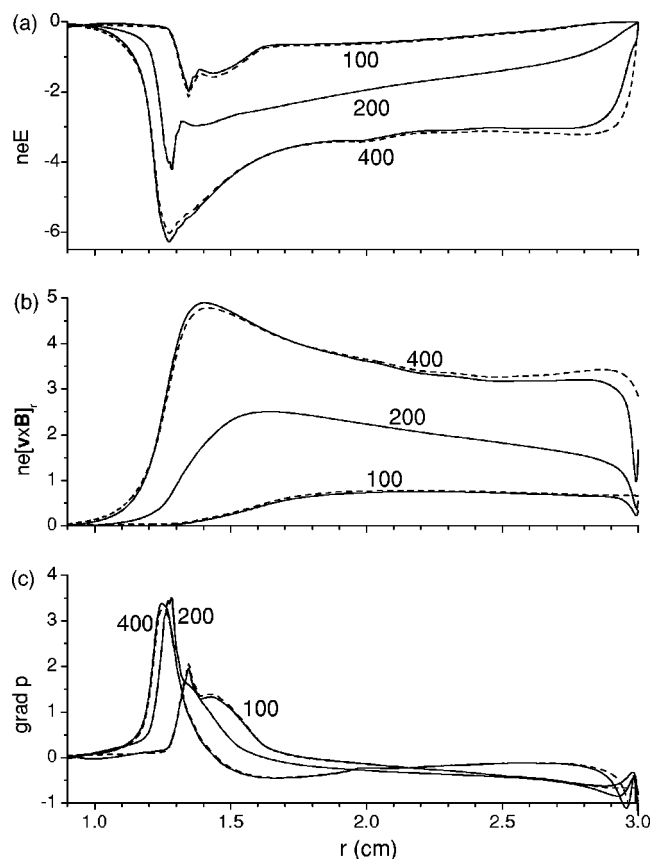

FIG. 7. Radial profiles of the electric field force (a), Lorentzian force (b), and isotropic pressure gradient (c) in units 10^{11} eV cm^{-4}. Full and broken lines are the results of the multiterm and two-term approximations, respectively. Numbers on curves indicate magnetic field strength in gauss.

term on the left hand side of Eq. (4)] becomes pronounced.

C. Anisotropy of electron pressure

Using the multiterm decomposition of the electron distribution function the problem of the electron pressure anisotropy can be analyzed.

By the tensor of total pressure of electrons we mean the quantity

$$\mathbf{P} = nm_e\langle\mathbf{vv}\rangle. \tag{12}$$

The electron velocity $\mathbf{v}$ is represented sometimes [12] as a sum of the directed $\mathbf{u}$ and random $\mathbf{w}$ velocities. The tensor of pressure $\mathbf{P}$ is then called the tensor of momentum flux and separated into two summands,

$$\mathbf{P} = nm_e\langle\mathbf{uu}\rangle + nm_e\langle\mathbf{ww}\rangle.$$

The first summand describes the momentum transport due to the directed motion. The second summand is called the pressure tensor and is separated, in turn, into the scalar isotropic pressure p and the viscous tension tensor. This approach is useful for hydrodynamic descriptions of particle transport.

In the framework of the kinetic description of electron motion it is more expedient to represent the total pressure
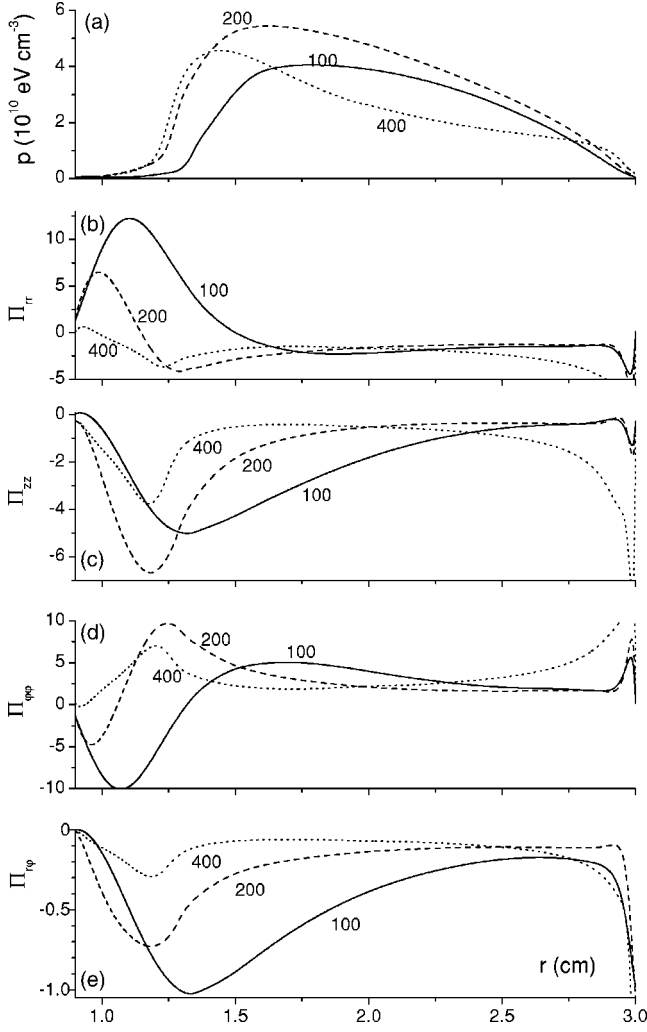
FIG. 8. Radial profiles of the isotropic pressure p (a) and the components of anisotropic pressure tensor: Π_{rr} (b), Π_{zz} (c), $\Pi_{\varphi\varphi}$ $=-(\Pi_{rr}+\Pi_{zz})$ (d), $\Pi_{r\varphi}$ (e) in units 10^8 eV cm^{-3}. Numbers on curves indicate magnetic field strength in gauss.

tensor (12) by a sum of the isotropic pressure tensor

$$p\mathbf{I} = nm_e\left\langle \frac{v^2}{3}\mathbf{I} \right\rangle = \frac{2}{3}nU_e\mathbf{I},$$

and the anisotropic pressure tensor

$$\mathbf{\Pi} = nm_e\left\langle \mathbf{vv} - \frac{v^2}{3}\mathbf{I} \right\rangle, \tag{13}$$

where $\mathbf{I}$ is the second rank identity tensor [9,13].

The tensor of anisotropic pressure was discussed in the preceding paper [8] along with the calculations of its components. The electron isotropic pressure and anisotropic pressure tensor components calculated by Eqs. (9), (10), and (11), are shown in Fig. 8.

The figures indicate that the isotropic pressure in the positive column exceeds the components of the tensor $\mathbf{\Pi}$ by two or three orders of magnitude. At the same time, the electron gas pressure is a fraction of the order of 10^{-4} of the neutral gas pressure. In the near-electrode regions a significant an-

isotropy of the electron pressure becomes apparent. The diagonal elements of the anisotropic pressure tensor Π_{rr}, Π_{zz}, and $\Pi_{\varphi\varphi}=-(\Pi_{rr}+\Pi_{zz})$ exceed noticeably the nondiagonal components $\Pi_{r\varphi}=\Pi_{\varphi r}$.

The anisotropy of the electron pressure can be demonstrated in the following way. The tensor of pressure can be represented as a surface of equal pressure and considered at any point with cylindrical coordinates r,φ,z of the cylindrical magnetron discharge in the basis of unit vectors $\mathbf{e}_r,\mathbf{e}_\varphi,\mathbf{e}_z$. For the isotropic pressure given by tensor $p\mathbf{I}$, this equipressure surface corresponds to a sphere of radius p. The normal to the surface of the sphere indicates the direction of the pressure force. In the presence of nonzero anisotropic components, the total pressure tensor (12) has the following form:

$$\mathbf{P} = \begin{pmatrix} p + \Pi_{rr} & \Pi_{r\varphi} & 0 \\ \Pi_{\varphi r} & p + \Pi_{\varphi\varphi} & 0 \\ 0 & 0 & p + \Pi_{zz} \end{pmatrix}. \tag{14}$$

If the nondiagonal elements of tensor (14) equal zero, the equipressure surface determined by this tensor is transformed into an ellipsoid with the semiaxes equal to

$$a_r = \Pi_{rr} + p, \quad a_\varphi = \Pi_{\varphi\varphi} + p, \quad a_z = \Pi_{zz} + p. \tag{15}$$

The presence of equal nondiagonal terms $\Pi_{r\varphi}=\Pi_{\varphi r}$ does not change the tensor's symmetry. A symmetrical tensor can be reduced to diagonal form by rotating the initial orthogonal basis $\mathbf{e}_r,\mathbf{e}_\varphi,\mathbf{e}_z$. The diagonalization method consists in finding the eigenvalues and eigenvectors of the tensor (14). Here, the second rank tensor's eigenvectors form a new basis with unit vectors $\mathbf{e}_r',\mathbf{e}_\varphi',\mathbf{e}_z'$, and the eigenvalues give the values of the diagonal elements. Projections of the eigenvectors on the unit vectors of the initial basis yield the angles of rotations. The pressure tensor (14) written in the new basis takes the diagonal form

$$\mathbf{P}' = \begin{pmatrix} (p + \Pi_{rr})' & 0 & 0 \\ 0 & (p + \Pi_{\varphi\varphi})' & 0 \\ 0 & 0 & (p + \Pi_{zz})' \end{pmatrix}. \tag{16}$$

As soon as the nondiagonal components of tensor $\mathbf{P}$ are considerably smaller than the diagonal ones (except for the points in the nearest vicinity of the anode), the magnitudes of the semiaxes of the ellipsoids $\mathbf{P}'$ and $\mathbf{P}$ at $\Pi_{r\varphi}=0$ differ a little. In the initial basis the ellipsoid given by the tensor $\mathbf{P}'$ (16), is rotated about the z axis in the plane (r,φ) by the angle $\alpha=\arccos(\mathbf{e}_r\cdot\mathbf{e}_r')$.

The semiaxis values of the pressure ellipsoid (16), normalized by the isotropic pressure $p(r)$, are shown in Fig. 9 for the cathode and anode regions where the anisotropy of pressure becomes especially apparent. In the positive column, as shown in the figure, the pressure of the electrons is almost isotropic: $a_r \approx a_\varphi \approx a_z \approx 1$.

Figure 10 demonstrates the cuts of the equipressure surfaces (ellipsoids of pressure) $\mathbf{P}'$ by the planes (r,φ), (r,z), and (z,φ) for two distinctive points in the cathode and anode regions marked in Fig. 9. Broken lines indicate the corresponding cuts of a sphere relevant to the isotropic pressure.
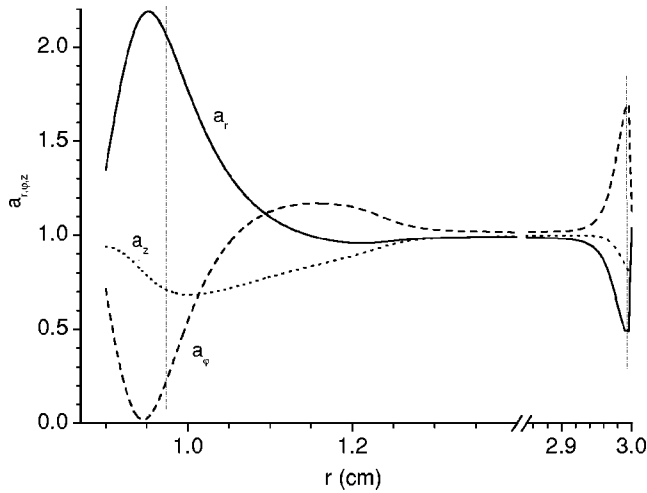
FIG. 9. Semiaxes of the ellipsoid of pressure **P**′, normalized by the isotropic pressure $p(r)$ in the cathode and anode regions at magnetic field strength $B=200$ G.

In the cathode region the ellipsoid of pressure is extended in the $\mathbf{e}_r$ direction and compressed in the $\mathbf{e}_z$ and especially in the $\mathbf{e}_\varphi$ directions. Rotation of the ellipsoid due to the presence of nondiagonal elements is negligible in this region. The deformation of the equipressure surface in the anode region is less pronounced. Here, the ellipsoid extends in the $\mathbf{e}_\varphi$ direction and contracts in the $\mathbf{e}_r$ and $\mathbf{e}_z$ directions. A rotation of the ellipsoid in the plane (r,φ) about the angle $\alpha \approx 5°$ is seen; this is caused by a relative increase of the nondiagonal elements $\Pi_{r\varphi}$ in comparison to the diagonal ones in the anode region.

D. Transport of energy

According to results obtained for the terms in the energy balance equation (2), divergence of the energy flux j_{ur} balances the power gain eEj_r in the cathode region and power
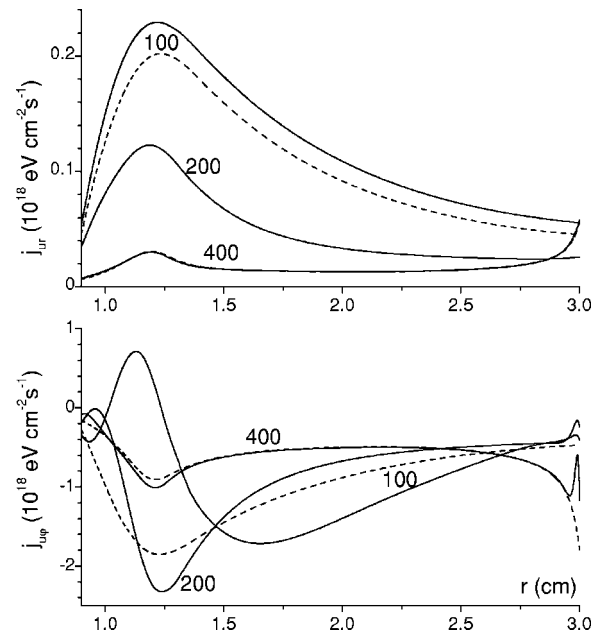

FIG. 11. Radial profiles of the radial j_{ur} and azimuth $j_{u\varphi}$ electron energy fluxes. Full and broken lines are the results of the multiterm and two-term approximations, respectively. Numbers on curves indicate magnetic field strength in gauss.

losses in collisions in the positive column. Power loss in elastic collisions H_{el} is small under low-pressure conditions compared with the power losses in ionization H_{io} and excitation H_{ex} collisions.

Azimuth components of the energy flux vector $j_{u\varphi}$ exceed, as a rule, the radial components j_{ur}. Figure 11 demonstrates the radial variation of the energy flux vector components. The discharge regions, where the azimuth components become equal to zero or change sign, are clearly seen. It is also seen that under strong anisotropy conditions (100 G) the two-term approximation is insufficient. The differences in radial dependencies of the energy and particle fluxes are seen
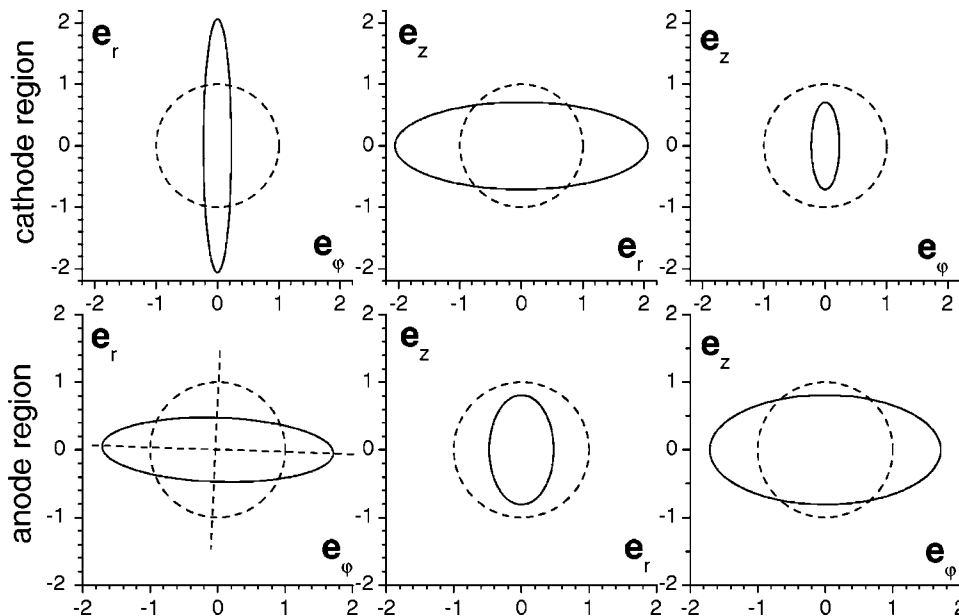

FIG. 10. Cuts of the ellipsoids of pressure by the principal planes in the cathode and anode regions at the points shown in Fig. 9. Broken lines are the cuts of the sphere corresponding to the isotropic pressure.

from comparison of Figs. 5 and 11; these are stipulated by large values of electron mean energy and small values of electron density in the cathode region. The power gain ej_rE is maximal near the cathode. For this reason, large energy fluxes are formed in the cathode region, with their values much exceeding those in the positive column. The situation for particle fluxes is opposite. The time of energy transport from cathode to anode is comparable with the time of the particle transport.

Using the radial and azimuth energy flux components the lines of energy flux can be constructed similarly to the lines of current shown in Fig. 6. In Fig. 12 the spiral lines of energy fluxes are shown in the transverse section of cylindrical magnetron discharge. As in the case of particles, a tangent to these curves defines the direction of the energy flux vector $\mathbf{j}_u$. It is seen from comparison with Fig. 6 that the numbers of loops of the energy flux lines are noticeably smaller than those of the spirals for particle flux. This is explained by the much smaller ratio of azimuth to radial components for energy flux in comparison with the corresponding ratio of the particle flux components. Distortions of the spiral lines seen in the cathode region at weak magnetic fields are similar to distortions in the lines of current; again this is due to a change of sign of azimuth component. A detailed study of this phenomena requires additional analysis employing higher-order terms.

The third rank tensor corresponding to the energy flux tensor

$$\mathbf{\Psi} = \frac{nm}{2}\langle \mathbf{vvv} - v^2\mathbf{Iv}\rangle \qquad (17)$$

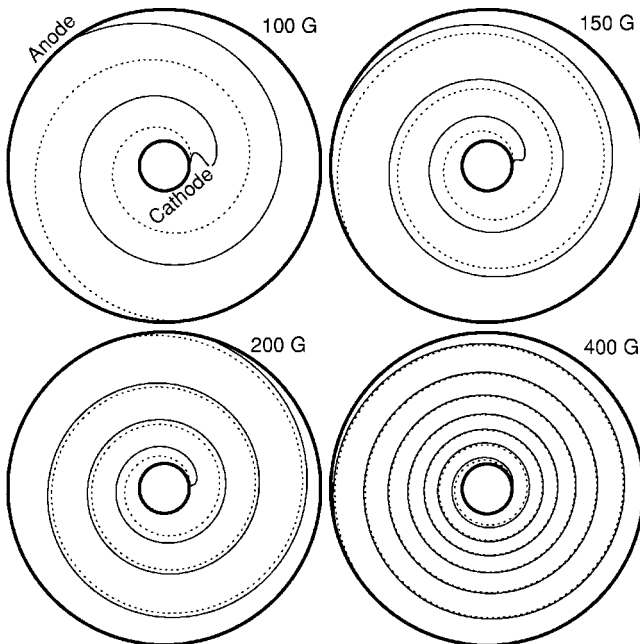consists of 27 components with six distinct nonzero components. Explicit expressions for the nonzero components are

given in [8]. The radial dependencies of these components are illustrated in Fig. 13.

This tensor has the property that a contraction with respect to any pair of indices equals zero: $\Psi_{rrr}+\Psi_{r\varphi\varphi}+\Psi_{rzz}=0$ and $\Psi_{\varphi rr}+\Psi_{\varphi\varphi\varphi}+\Psi_{\varphi zz}=0$. Under anisotropic conditions the tensor components with r the first index influence the magnitude and direction of the radial component of the energy flux vector j_{ur}, and those with φ the first index influence the azimuth part $j_{u\varphi}$. The role of anisotropy in energy transport is important, as soon as the absolute values of the energy flux tensor components are comparable to or even exceed those for the energy flux vector; this can be seen by comparing the corresponding quantities shown in Figs. 11 and 13. In
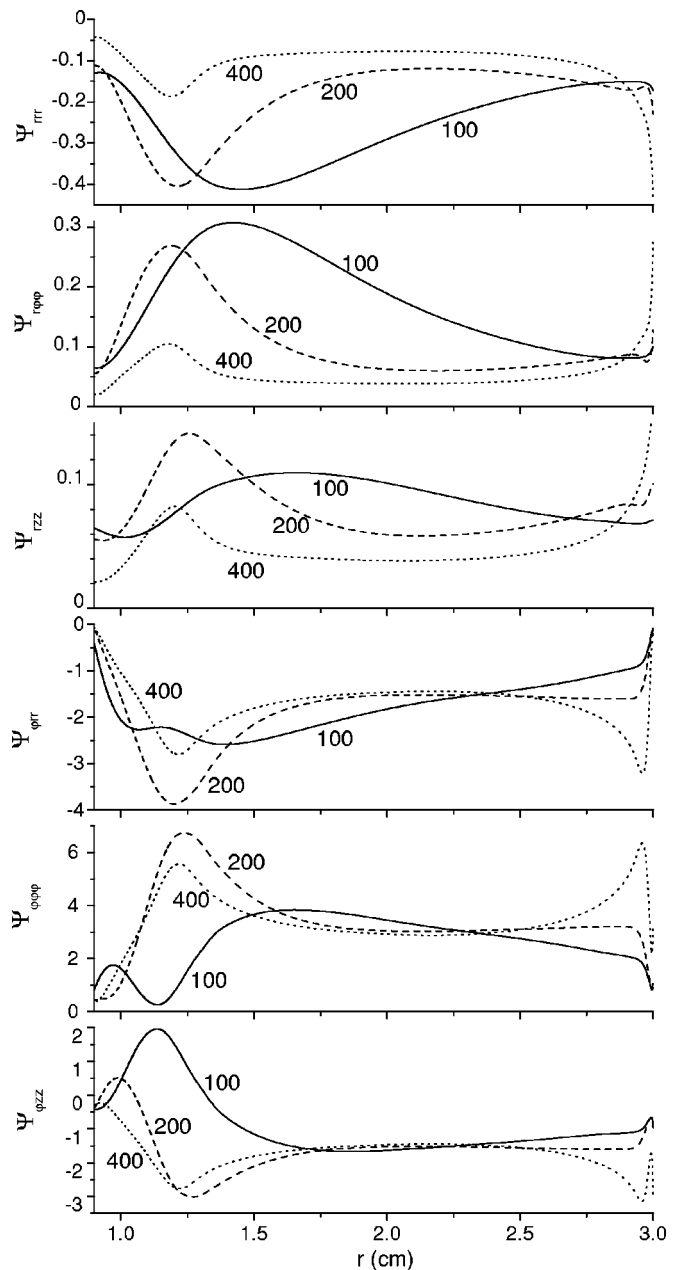

FIG. 12. Lines of electron energy flux in the plane $z=$const of the cylindrical magnetron discharge at different magnetic field strengths. Multiterm approximation (full lines) is compared with the two-term approximation (broken lines).

FIG. 13. Radial profiles of the energy flux tensor components in units of 10^{18} eV cm^{-2} s^{-1}. Numbers on curves indicate magnetic field strength in gauss.

contrast to strong anisotropy in energy transport, it is weak in the transport of momentum, which follows from the smallness of the anisotropic pressure tensor components (Fig. 8) in comparison with the isotropic pressure.

Thus, the transport processes of particles, momentum, and energy are considered for the cathode and anode regions, and the positive column of the cylindrical magnetron discharge.

V. CONCLUSION

A general theory for multiterm decomposition of the phase space distribution function in terms of the spherical tensors is applied to describe the electron component in a cylindrical magnetron discharge in argon. The distribution functions and macroscopic quantities are calculated at various magnetic and electric fields corresponding to those measured in experiments. The presence of an undulating structure in the distribution functions at weak magnetic fields is demonstrated along with its flattening at larger fields. The undulating structure at low magnetic field strengths is stipulated by the relaxation of an initial high-energy swarm of electrons ejected from the cathode surface and by the nonlocal character of the distribution function formation. This structure is flattened due to the distribution localization with increasing magnetic field strength.

The balance equations for particles, radial and azimuth momenta, and energy are considered with a discussion of the main channels for the momentum and energy gain and loss.

Spiral trajectory lines are obtained to give a visual illustration for the directed particle and energy transport in the radial planes of the cylindrical magnetron discharge. The phenomenon of electron pressure anisotropy is considered. The equipressure surface under conditions of noticeable anisotropy, in electrode regions for instance, is shown to transform from a sphere, corresponding to the isotropic pressure, into an ellipsoid. A method to calculate the values of the ellipsoid's semiaxes and the rotation angles is suggested. The variation of the semiaxis values is shown in dependence on the radial position. Additionally, the components of the energy flux vector and tensor are computed and a strong anisotropy in the energy flux transport found.

Application of the multiterm theory developed in [9] and generalized with respect to cylindrical magnetron discharge in [8] permitted us to study many interesting phenomena that were beyond the scope of the conventional two-term approximation. Taking higher-order decomposition terms into account will be useful for future investigations of the solution convergence and the effect of higher expansion coefficients on the phenomena caused by the anisotropy.

[1] P. Kudrna, M. Holik, and M. Tichy, Czech. J. Phys. **52**, Suppl. A, D666 (2002).

[2] P. Kudrna, M. Tichy, J. F. Behnke, C. Csambal, and J. Rusz, in Proceedings of the 15th ISPC, Orleans, France, edited by A. Bouchole *et al.* (Gremy Laboratory, Orleans, France, 2001), Vol. 4, p. 2119.

[3] M. Holik *et al.*, in Proceedings of the XXVIth ICPIG, Greifswald, Germany, edited by J. Meichsner *et al.* (Local Organizing Committee, Greifswald, 2003), Vol. 2, p. 43.

[4] T. A. van der Straaten, N. F. Cramer, I. S. Falconer, and B. W. James, J. Phys. D **31**, 191 (1998).

[5] I. A. Porokhova, Yu. B. Golubovskii, J. Bretagne, M. Tichy, and J. F. Behnke, Phys. Rev. E **63**, 056408 (2001).

[6] I. A. Porokhova, Yu. B. Golubovskii, M. Holik, P. Kudrna, M. Tichy, C. Wilke, and J. F. Behnke, Phys. Rev. E **68**, 016401 (2003).

[7] I. A. Porokhova, Yu. B. Golubovskii, C. Csambal, V. Helbig, C. Wilke, and J. F. Behnke, Phys. Rev. E **65**, 046401 (2002).

[8] I. A. Porokhova, Yu. B. Golubovskii, and J. F. Behnke, preceding paper, Phys. Rev. E **71**, 066406 (2005).

[9] R. E. Robson, R. Winkler, and F. Sigeneger, Phys. Rev. E **65**, 056410 (2002).

[10] D. U. von Rosenberg, *Methods for the Numerical Solutions of Partial Differential Equations* (American Elsevier, New York, 1971).

[11] R. D. White, R. E. Robson, B. Schmidt, and M. A. Morrison, J. Phys. D **36**, 3125 (2003).

[12] V. E. Golant, A. P. Zhilinsky, I. E. Sakharov, and S. C. Brown, *Fundamentals of Plasma Physics* (Wiley, New York, 1980).

[13] I. P. Shkarofsky, T. W. Johnston, and M. P. Bachynski, *The Particle Kinetics of Plasmas* (Addison-Wesley, Reading, MA, 1966).